Adaptive Robust Control of Multi-DOF Hydraulic Manipulator with Precise Online Load Estimation

Qixian Wang[1,2], Manzhi Qi[1,2], Yangxiu Xia[1,2], Shizhao Zhou[1,2], Zheng Chen[1,2,*]

[1] State Key Laboratory of Fluid Power and Mechatronic Systems, Zhejiang University, Hangzhou 310027, China

[2] Ocean College, Zhejiang University, Zhoushan, Zhejiang, 316021, China

*Corresponding author: E-mail: zheng_chen@zju.edu.cn

Contributing authors: qxwang_m@zju.edu.cn; manzhi.q@zju.edu.cn; yx.xia@zju.edu.cn; zhoushizhao@zju.edu.cn.

Abstract

The hydraulic manipulator has broad application prospects in heavy load working conditions. However, compared with electric manipulators, achieving high control precision in existing hydraulic manipulators presents a greater challenge. This is primarily due to factors such as joint coupling, heavy payload, uncertainties, and the complexities of high-order nonlinear dynamics. Additionally, the unknown load mass plays a crucial role in influencing the accuracy of the control system. In various work settings, accurately determining the load is a significant concern. However, precise measurement of load mass often becomes demanding due to the absence of adequate force or torque sensors. In this paper, a new load estimation method based on direct/indirect adaptive robust controller (DIARC) is proposed. To ensure accurate, real-time payload estimation under dynamic conditions, a backstepping strategy coupled with a recursive least square adaptive law is employed. By integrating this accurately estimated load mass into the control system, an enhancement in overall control performance can be achieved. The effectiveness of this enhanced controller with load mass estimation is analyzed and validated on a four-degree-of-freedom hydraulic

manipulator. The results demonstrate that our proposed method successfully achieves precise online load mass estimation, and results in an enhanced control performance.

Keywords: Hydraulic manipulator, Adaptive control, Load estimation.

1. Introduction

Hydraulic drive systems are extensively utilized in various industrial sectors, including oil and gas production, mining industries, civil engineering industries, and aerospace [1-3]. As industrial automation continues to advance, the demand for precision in various work settings, such as collaborative pipeline assembly and equipment maintenance, is on the rise [4]. Multi-degree-of-freedom (DOF) hydraulic manipulators, serving as intelligent hydraulic equipment, are increasingly crucial in these varied environments [5]. However, their application remains constrained due to the lower control precision they offer compared to electric manipulators [6, 7].

Compared with other hydraulic systems, hydraulic manipulators necessitate enhanced control accuracy to effectively handle more complex tasks. A key factor contributing to their reduced control performance is intricate dynamic characteristics. The hydraulic system, comprising components like proportional valves and servo valves, often introduces high-order nonlinearities, including Coulomb friction, viscous friction, and various unknown external disturbances [8-10]. These complexities pose a significant challenge for PID controllers in achieving high control accuracy [11, 12]. To improve the control accuracy of hydraulic system, many researches were carried out. Shen e*t al*. proposed an adaptive integral terminal sliding mode controller to guarantee the robustness of double-variable hydraulic transformer and effectively improved the control effect [13]. B. Yao and Chen e*t al*. proposed an adaptive robust motion control theory to deal with the control of single-rod hydraulic actuators and the parameter uncertainty and uncertain nonlinearity of cylinder control systems [14-17]. J. Yao e*t al*.

conducted extensive research on the parameter uncertainty of hydraulic systems and combined the RISE-based controller with online parameter adaptive law to effectively suppress parameter uncertainty and reduce tracking errors of hydraulic systems [18-21]. Hou *et al.* proposed a force-free control method for compensating for friction, gravity, and inertia of hydraulic Stewart manipulators. By using separate compensation and complete compensation methods, the force-free control of the Stewart mechanism was achieved and good control effects were obtained on parallel robots [22]. While the aforementioned methods have achieved good control performance on the single hydraulic actuator platform, more complex control challenge remains on the multi-DOF hydraulic manipulators which is also limited by joint coupling, system inertia, fluid dynamics and other factors [5, 23]. Mattila *et al.* proposed the virtual decomposition control (VDC) method for multi-DOF hydraulic manipulators [24-26]. Ahn *et al.* proposed a sliding mode control algorithm using a finite-time disturbance observer [27] for a 3-DOF hydraulic manipulator considering the actuator dynamics and the joint tracking errors were guaranteed to converge to zero in finite time under the strong assumption that the uncertain joint dynamics were time invariant.

Another factor impacting accuracy is the unknown load mass at the end effector. In many demanding and harsh operational environments, implementing force/torque sensors at the end effectors for accurate load mass measurement is challenging. Given that the hydraulic manipulator's load is not only time-varying but typically large, this significantly influences the manipulator's dynamic characteristics. Consequently, there is a pressing need for precise online load estimation that can effectively compensate for this unknown load. Furthermore, such online load estimation is essential in sectors like workpiece handling and cargo sorting, where the awareness of payload mass is crucial. Many studies investigated the unknown load changes of machinery. Lin *et al.* developed

a load sensing system based on displacement adaptive and variable speed control for electric hydraulic excavator, considerably improving its control performance [28]. Duan *et al.* proposed a variable structure robust control method based on equivalent control and a feedforward compensator for robots with load uncertainty, achieving better control effects under the condition of no force sensor at the end effector [29]. Sun *et al.* analyzed a novel natural adaption law which achieved accurate control for redundant manipulators when picking tools with unknown length, direction, and mass, and the parameter estimation speed was also increased [30]. Zeng *et al.* and Colomé *et al.* explored methods for estimating the load conditions of electric rigid manipulators [31, 32]. Bartlett *et al.* and Tessari *et al.* considered the parameter uncertainty of load mass for single-rod hydraulic knee prostheses [33, 34]. Renner *et al.* proposed online payload estimation method and achieved high estimation performance in earthmoving excavator [35]. However, more research on load compensation and estimation of hydraulic manipulator is needed.

In this paper, we introduce a Direct/Indirect Adaptive Robust Controller (DIARC) to achieve real-time load estimation and improve the control precision of hydraulic manipulators. This controller is specifically designed to mitigate the effects of model nonlinearity and unknown external disturbances, while simultaneously maintaining system stability. Additionally, the load is integrated into the model as a state variable, and a parameter estimation method is employed to ensure accurate load estimation. Through this approach, the controller and load estimator are combined, allowing for a complementary enhancement in both control and estimation accuracy. As well, this strategy not only achieves computational efficiency but also results in cost savings.

2. Problem formulation

2.1. Dynamic modeling of hydraulic manipulator

The schematic diagram of a multi-DOF manipulator is shown in Fig. 1. For the convenience of dynamic modeling, it is supposed that the centroid of each link is at its center. Therefore, the dynamic model of a *n*-DOF manipulator is established using Lagrange method as:

$$\boldsymbol{M}(q)\ddot{\boldsymbol{q}} + \boldsymbol{C}(q,\dot{q})\dot{\boldsymbol{q}} + \boldsymbol{G}(q) + \boldsymbol{F}_c\boldsymbol{s}(\dot{q}) + \boldsymbol{F}_v\dot{\boldsymbol{q}} = \boldsymbol{\tau} + \boldsymbol{D}_1 \tag{1}$$

where $\boldsymbol{F}_c = diag(F_{c1}, F_{c2}, \cdots, F_{cn})$ and $\boldsymbol{F}_v = diag(F_{v1}, F_{v2}, \cdots, F_{vn})$ are the Coulomb friction coefficient and viscous friction coefficient, respectively. $\boldsymbol{D}_1 \in \mathbb{R}^n$ is the matrix of modeling uncertainty. The joint control torque $\boldsymbol{\tau} \in \mathbb{R}^n$ is calculated by

$$\begin{aligned} \boldsymbol{\tau} &= \boldsymbol{\mu}\boldsymbol{F}_L \\ \boldsymbol{F}_L &= \boldsymbol{P}_1\boldsymbol{A}_1 - \boldsymbol{P}_2\boldsymbol{A}_2 \end{aligned} \tag{2}$$

where $\boldsymbol{\mu} = \partial\boldsymbol{l} / \partial\boldsymbol{q}$ is the joint Jacobian matrix, $\boldsymbol{l} \in \mathbb{R}^n$ is the length of the cylinders, $\boldsymbol{F}_L \in \mathbb{R}^n$ is the control thrust of the hydraulic cylinders, $\boldsymbol{A}_1 \in \mathbb{R}^n$ and $\boldsymbol{P}_1 = diag(p_{11}, p_{12}, \cdots, p_{1n})$ represent the area and pressure of the cylinders with rod, $\boldsymbol{A}_2 \in \mathbb{R}^n$ and $\boldsymbol{P}_2 = diag(p_{21}, p_{22}, \cdots, p_{2n})$ represent the area and pressure of the cylinders without rod. The matrix of inertial $\boldsymbol{M} \in \mathbb{R}^{n\times n}$, the matrix of Coriolis force and centrifugal force $\boldsymbol{C} \in \mathbb{R}^{n\times n}$ and the matrix of gravity $\boldsymbol{G} \in \mathbb{R}^n$ can be written as:

$$\begin{aligned} &\boldsymbol{M}(q) = \boldsymbol{M}_1(q) + \boldsymbol{M}_t(q)m_t,\ \boldsymbol{C}(q,\dot{q}) = \boldsymbol{C}_1(q,\dot{q}) + \boldsymbol{C}_t(q,\dot{q})m_t \\ &\boldsymbol{G}(q) = \boldsymbol{G}_1(q) + \boldsymbol{G}_t(q)m_t \end{aligned} \tag{3}$$

where $\boldsymbol{M}_t$, $\boldsymbol{C}_t$ and $\boldsymbol{G}_t$ represent additional terms generated due to the unknown load mass. Their detailed expression can be found in the appendix.

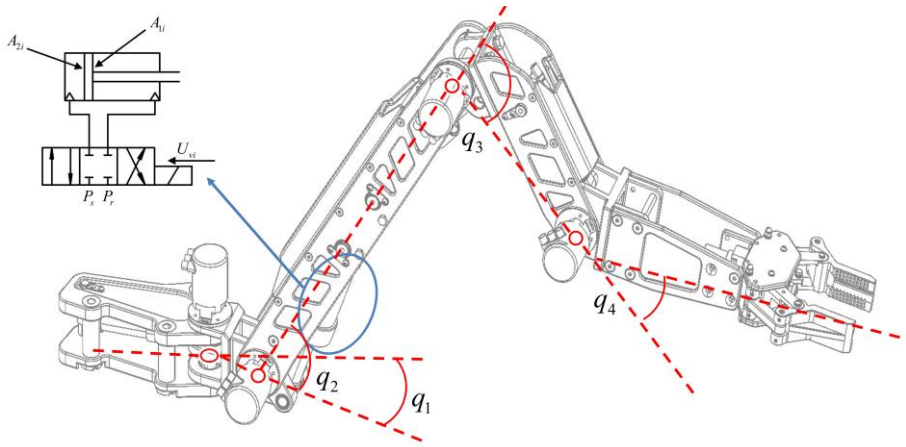

Fig. 1. Schematic diagram of the manipulator

According to Ref [36], the joint dynamics model can be expressed as:

$$\beta_e^{-1}\dot{\boldsymbol{F}}_L = -\boldsymbol{A}_Q\boldsymbol{\mu}\dot{\boldsymbol{q}} + \boldsymbol{Q}_L + \boldsymbol{D}_2 \tag{4}$$

where β_e is the elastic bulk modulus of hydraulic oil, $\boldsymbol{D}_2 \in \mathbb{R}^n$ is the modeling uncertainty.

The following static mapping can describe the relationship between $Q_{Li}(i=1,2,\cdots,n)$ and valve control voltage $U_{vi}(i=1,2,\cdots,n)$ as follows:

$$\begin{aligned} U_{vi} &= \frac{Q_{Li}/k_v}{(A_{1i}/V_{1i})k_{Q_1}\sqrt{(\Delta \mathrm{P}_{1i})}+(A_{2i}/V_{2i})k_{Q_2}\sqrt{(\Delta \mathrm{P}_{2i})}}, i=1,2,\cdots,n \\ \Delta \mathrm{P}_{1i} &= \begin{cases} p_{si}-p_{1i}, U_v \geq 0 \\ p_{1i}-p_{ri}, U_v<0 \end{cases}, \Delta \mathrm{P}_{2i} = \begin{cases} p_{2i}-p_{ri}, U_v \geq 0 \\ p_{si}-p_{2i}, U_v<0 \end{cases} \end{aligned} \tag{5}$$

where k_{Q1} and k_{Q2} are the flow gain coefficient of the valve, k_v the linearized flow gain of the valve, p_{si} and p_{ri} the supply pressure and the reference pressure of the i^{th} cylinder respectively. $\boldsymbol{V}_1 = diag(V_{11},V_{12},\cdots,V_{1n})$ and $\boldsymbol{V}_2 = diag(V_{21},V_{22},\cdots,V_{2n})$ denote the volumes of the cylinders with and without rod respectively.

2.2.Parameterization of the dynamic model

Parameters such as the mass, moment of inertia, and coefficient of friction of the joints are unknown. Hydraulic systems also have the characteristics of uncertainty and nonlinearity. To facilitate subsequent controller design, the unknown parameters and

nonlinearities are parameterized as:

$$\begin{cases} \boldsymbol{\theta} = [m_t, \beta_e^{-1}, \vartheta_1, \vartheta_2, \vartheta_3, \vartheta_4, \vartheta_5]^T,\ \boldsymbol{\theta} \in \mathbb{R}^{5n+2} \\ \vartheta_i = [\pi_1(i), \cdots, \pi_j(i), \cdots, \pi_n(i)],\ i = 1,2,\cdots,5 \\ \pi_j = [m_j, F_{cj}, F_{vj}, D_{1cj}, D_{2cj}],\ j = 1,2,\cdots,n \end{cases} \tag{6}$$

where $\vartheta_i \in \mathbb{R}^n$ represents the parameter set of the i^{th} physical parameter in n DOF, $\pi_j \in \mathbb{R}^6$ represents the parameter set of the j^{th} DOF and $m_j (j = 1,2,\cdots,n)$ is the mass of the j^{th} link. For parameters that only appear once in the parameter set, defining $\theta_1 = m_t$, $\theta_2 = \beta_e^{-1}$. In Eq.6, $\boldsymbol{D}_{ic} = \boldsymbol{D}_i - \Delta\boldsymbol{D}_i = [D_{ic1}, D_{ic2}, \cdots D_{icn}](i = 1,2)$ is the low frequency calculable part of $\boldsymbol{D}_i$.

The general dynamics and the hydraulic dynamics of the manipulator have the following properties.

Property 1

For a certain form of $\boldsymbol{\theta}$, the general dynamics and the hydraulic dynamics of the manipulator can be expressed in the form of linear regression as follows:

$$\boldsymbol{\tau} = \boldsymbol{\varphi}_1^T \boldsymbol{\theta} + \Delta\boldsymbol{D}_1 \tag{7}$$

$$\theta_2 \dot{\boldsymbol{F}}_L = -\boldsymbol{A}_Q \boldsymbol{\mu} \dot{\boldsymbol{q}} + \boldsymbol{Q}_L + \boldsymbol{\varphi}_2^T \boldsymbol{\theta} + \Delta\boldsymbol{D}_2 \tag{8}$$

where $\boldsymbol{\varphi}_i (i = 1,2)$ are linear regression matrixes, $\Delta\boldsymbol{D}_i (i = 1,2)$ the incalculable part of $\boldsymbol{D}_i$.

Assumption 1

Due to the boundary limitations of the above unknown quantities in practice, the following assumptions can be made:

$$\begin{aligned} &\theta_i \in \Omega_{\theta_i} \triangleq \{\theta_i : \theta_{imin} \le \theta_i \le \theta_{imax}\}, i = 1,2,\ldots,5n+2 \\ &\left\|\Delta D_i\right\| \le \delta_i, i = 1,2,3 \end{aligned} \tag{9}$$

where δ_i is a known vector. And all parameters are unknown but slowly changing or constant.

2.3. Control objective

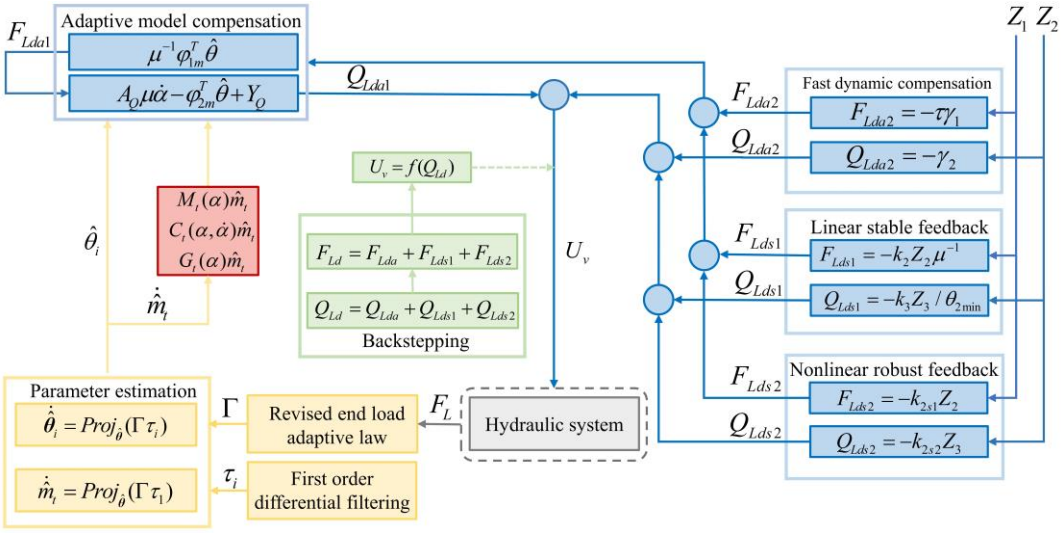

Fig. 2. The algorism diagram of the controller

The first target is in this paper to generate the valve control voltage U_{vi} in Eq. 5. Therefore, the tracking accuracy of each joint of the manipulator can be achieved, despite noise and unknown load mass. The second target is to make precise estimation of the unknown load mass in a comparatively short time, *i.e.*, to make θ_1 converge to its real value.

3. Control of the manipulator

3.1. Controller design

The algorism diagram of DIARC controller is shown in Fig. 2. Backstepping strategy is adopted to cope with the uncertainty and nonlinearity of hydraulic dynamics.

STEP I.

The angular error is defined as:

$$\boldsymbol{Z}_1 = \boldsymbol{q} - \boldsymbol{q}_d \in \mathbb{R}^n \tag{10}$$

where $\boldsymbol{q} \in \mathbb{R}^n$ is the actual angle of each joint, and $\boldsymbol{q}_d \in \mathbb{R}^n$ the desired angle of each joint.

The angular velocity error is thus defined as:

$$\boldsymbol{Z}_2 = \dot{\boldsymbol{Z}}_1 + \boldsymbol{k}_1\boldsymbol{Z}_1 = \dot{\boldsymbol{q}} - \dot{\boldsymbol{q}}_{eq},\ \dot{\boldsymbol{q}}_{eq} = \dot{\boldsymbol{q}}_d - \boldsymbol{k}_1\boldsymbol{Z}_1 \tag{11}$$

$$\dot{\boldsymbol{Z}}_2 = \ddot{\boldsymbol{q}} - \ddot{\boldsymbol{q}}_{eq} \tag{12}$$

where $\boldsymbol{Z}_2 \in \mathbb{R}^n$ and $\boldsymbol{k}_1 \in \mathbb{R}^{n\times n}$ are a positive definite diagonal matrix.

Then, the control object is to make $\boldsymbol{Z}_2$ converge to 0. Based on property 1, Eq.1 can equally be written as:

$$\boldsymbol{M}(q)\ddot{\boldsymbol{q}}_{eq} + \boldsymbol{C}(q,\dot{q})\dot{\boldsymbol{q}}_{eq} + \boldsymbol{G}(q) + \boldsymbol{F}_c\boldsymbol{s}(\dot{q}) + \boldsymbol{F}_s\dot{\boldsymbol{q}} = \boldsymbol{\varphi}_{1m}^T\boldsymbol{\theta} + \boldsymbol{D}_{1c} \tag{13}$$

where $\boldsymbol{\varphi}_{1m}$ is also a linear regression matrix.

Eq.1 minus Eq.13 and consider Eq.2, we can get:

$$\boldsymbol{M}(q)\dot{\boldsymbol{Z}}_2 + \boldsymbol{C}(q,\dot{q})\boldsymbol{Z}_2 = -\boldsymbol{\varphi}_{1m}^T\boldsymbol{\theta} + \boldsymbol{\mu}\boldsymbol{F}_L + \Delta\boldsymbol{D}_1 \tag{14}$$

Let $\hat{\bullet}$ represent the estimation of $\bullet$, and $\tilde{\bullet} = \hat{\bullet} - \bullet$ is the error between the real value and the estimation. Similar to tracking error, we further design virtual control thrust $\boldsymbol{F}_{Ld}$, which can be dismantled into the following parts:

$$\begin{aligned} &\boldsymbol{F}_{Ld} = \boldsymbol{F}_{Lda} + \boldsymbol{F}_{Lds},\ \boldsymbol{F}_{Lda} = \boldsymbol{F}_{Lda1} + \boldsymbol{F}_{Lda2},\ \boldsymbol{F}_{Lds} = \boldsymbol{F}_{Lds1} + \boldsymbol{F}_{Lds2} \\ &\boldsymbol{F}_{Lda1} = \boldsymbol{\mu}^{-1}\boldsymbol{\varphi}_{1m}^T\hat{\boldsymbol{\theta}},\ \boldsymbol{F}_{Lds1} = -\boldsymbol{k}_2\boldsymbol{\mu}^{-1}\boldsymbol{Z}_2 \end{aligned} \tag{15}$$

where $\boldsymbol{F}_{Ld} \in \mathbb{R}^n$ is the virtual force input. $\boldsymbol{F}_{Lda1}$ is designed to compensate nonlinearities. $\boldsymbol{F}_{Lda2}$ is the fast-dynamic compensation item which will be designed in STEP II. $\boldsymbol{F}_{Lds1}$ can keep the system stable if $\boldsymbol{k}_2 \in \mathbb{R}^{n\times n}$ is a positive definite diagonal matrix. $\boldsymbol{F}_{Lds2}$ is set to compensate the parameter uncertainties, which be designed in STEP II. If we nominate the force tracking error as Eq.16, according to Eqs.14 and 15, the derivatives of $\boldsymbol{Z}_2$ can be written as:

$$\boldsymbol{Z}_3 = \boldsymbol{F}_L - \boldsymbol{F}_{Ld},\ \boldsymbol{Z}_3 \in \mathbb{R}^n \tag{16}$$

$$\boldsymbol{M}(q)\dot{\boldsymbol{Z}}_2 + \boldsymbol{C}(q,\dot{q})\boldsymbol{Z}_2 = -\boldsymbol{\varphi}_{1m}^T\tilde{\boldsymbol{\theta}} + \boldsymbol{\mu}\boldsymbol{Z}_3 - \boldsymbol{k}_2\boldsymbol{Z}_2 + \boldsymbol{\mu}(\boldsymbol{F}_{Lda2} + \boldsymbol{F}_{Lds2}) + \Delta\boldsymbol{D}_1 \tag{17}$$

STEP II.

Based on Eq.8, the derivatives of $\boldsymbol{Z}_3$ can be further expressed as:

$$\begin{aligned}\theta_2\dot{\boldsymbol{Z}}_3 &= \theta_2\dot{\boldsymbol{F}}_L - \theta_2\dot{\boldsymbol{F}}_{Ld} \\ &= -\boldsymbol{A}_Q\boldsymbol{\mu}\dot{\boldsymbol{q}} + \boldsymbol{Q}_L + \boldsymbol{\varphi}_2^T\boldsymbol{\theta} - \theta_2\dot{\boldsymbol{F}}_{Ld} + \Delta\boldsymbol{D}_2\end{aligned} \tag{18}$$

$\dot{\boldsymbol{F}}_{Ld}$ can be dismantled into the calculable part $\dot{\boldsymbol{F}}_{Ldc}$ and the incalculable part $\dot{\boldsymbol{F}}_{Ldi}$, that is:

$$\dot{\boldsymbol{F}}_{Ld} = \dot{\boldsymbol{F}}_{Ldc} + \dot{\boldsymbol{F}}_{Ldi},\ \dot{\boldsymbol{F}}_{Ldc} = \frac{\partial \boldsymbol{F}_{Ld}}{\partial \boldsymbol{q}}\dot{\boldsymbol{q}} + \frac{\partial \boldsymbol{F}_{Ld}}{\partial \dot{\boldsymbol{q}}}\hat{\dot{\boldsymbol{q}}} + \frac{\partial \boldsymbol{F}_{Ld}}{\partial t},\ \dot{\boldsymbol{F}}_{Ldi} = \frac{\partial \boldsymbol{F}_{Ld}}{\partial \dot{\boldsymbol{q}}}(\ddot{\boldsymbol{q}} - \hat{\ddot{\boldsymbol{q}}}) + \frac{\partial \boldsymbol{F}_{Ld}}{\partial \hat{\boldsymbol{\theta}}}\dot{\hat{\boldsymbol{\theta}}} \tag{19}$$

where $\hat{\ddot{\boldsymbol{q}}}$ is the estimated value of $\ddot{\boldsymbol{q}}$.

If we consider Eq.19, Eq.18 can be expressed as:

$$\theta_2\dot{\boldsymbol{Z}}_3 = -\boldsymbol{A}_Q\boldsymbol{\mu}\dot{\boldsymbol{q}} + \boldsymbol{Q}_L + \boldsymbol{\varphi}_{2m}^T\boldsymbol{\theta} - \theta_2\dot{\boldsymbol{F}}_{Ldi} + \Delta\boldsymbol{D}_2 \tag{20}$$

Similar to the design of virtue forth input, virtual flow input $\boldsymbol{Q}_{Ld} \in \mathbb{R}^n$ can be written as:

$$\begin{aligned}&\boldsymbol{Q}_{Ld} = \boldsymbol{Q}_{Lda} + \boldsymbol{Q}_{Lds},\ \boldsymbol{Q}_{Lda} = \boldsymbol{Q}_{Lda1} + \boldsymbol{Q}_{Lda2},\ \boldsymbol{Q}_{Lds} = \boldsymbol{Q}_{Lds1} + \boldsymbol{Q}_{Lds2} \\ &\boldsymbol{Q}_{Lda1} = \boldsymbol{A}_Q\boldsymbol{\mu}\dot{\boldsymbol{q}} - \boldsymbol{\varphi}_{2m}^T\hat{\boldsymbol{\theta}} + \boldsymbol{Y}_Q,\ \boldsymbol{Q}_{Lds1} = -\frac{\boldsymbol{k}_3}{\theta_{2\max}}\boldsymbol{Z}_3\end{aligned} \tag{21}$$

In Eq.21, $\boldsymbol{Q}_{Lda1}$ is designed to compensate nonlinearities, while $\boldsymbol{Q}_{Lda2}$ is the fast-dynamic compensation item. $\boldsymbol{Q}_{Lds1}$ can keep the system stable if $\boldsymbol{k}_3 \in \mathbb{R}^{n\times n}$ is a positive definite diagonal matrix. $\boldsymbol{Q}_{Lds2}$ is set to compensate the parameter uncertainties, which will be designed later. $\boldsymbol{Y}_Q = -\boldsymbol{\mu}\boldsymbol{Z}_2\boldsymbol{\omega}_1 / \boldsymbol{\omega}_2$ is the backstepping compensating item, Due to the fact that $\boldsymbol{Z}_2$ and $\boldsymbol{Z}_3$ may not be of the same order of magnitude in practice, we introduce $\boldsymbol{\omega}_1 = diag(\omega_{11},\cdots,\omega_{1n}) \in \mathbb{R}^{n\times n}$ and $\boldsymbol{\omega}_2 = diag(\omega_{21},\cdots,\omega_{2n}) \in \mathbb{R}^{n\times n}$ to balance their magnitudes and compensate the extra item in subsequent Lyapunov stability analysis. Based on Eqs.20 and 21, $\dot{\boldsymbol{Z}}_3$ can be described as:

$$\theta_2 \dot{\boldsymbol{Z}}_3 = -\boldsymbol{\varphi}_{2m}^T \tilde{\boldsymbol{\theta}} + \boldsymbol{k}_3 \boldsymbol{Z}_3 \frac{1}{\theta_{2\max}} - \boldsymbol{Y}_Q + \boldsymbol{Q}_{Lda2} + \boldsymbol{Q}_{Lds2} - \theta_2 \dot{\boldsymbol{F}}_{Ldi} + \Delta \boldsymbol{D}_2 \tag{22}$$

Since $\boldsymbol{k}_3$ is a positive definite diagonal matrix. $\boldsymbol{Z}_3$ can converge to 0 if the small quantities are ignored.

So far, the stability of the system is ensured and the compensation of nonlinearities is completed. Now, design $\boldsymbol{F}_{Lda2}$ and $\boldsymbol{Q}_{Lda2}$ as fast-dynamic compensation items. They will play a significant role in reducing the dynamic error. The modeling uncertainty and parameter estimation error in Eqs.17 and 22 can be divided into the low frequency part $\boldsymbol{d}_i \in \mathbb{R}^n$ and high frequency part $\tilde{\boldsymbol{d}}_i \in \mathbb{R}^n (i = 1,2)$, that is:

$$\begin{cases} \boldsymbol{d}_1 + \tilde{\boldsymbol{d}}_1^* = -\boldsymbol{\varphi}_{1m}^T \tilde{\boldsymbol{\theta}} + \Delta \boldsymbol{D}_1 \\ \boldsymbol{d}_2 + \tilde{\boldsymbol{d}}_2^* = -\boldsymbol{\varphi}_{2m}^T \tilde{\boldsymbol{\theta}} - \theta_2 \dot{\boldsymbol{F}}_{Ldi} + \Delta \boldsymbol{D}_2 \end{cases} \tag{23}$$

Fast dynamic compensation items can thus be designed as:

$$\begin{cases} \boldsymbol{F}_{Lda2} = -\boldsymbol{\mu}^{-1} \hat{\boldsymbol{d}}_1 \\ \boldsymbol{Q}_{Lda2} = -\hat{\boldsymbol{d}}_2 \end{cases} \tag{24}$$

where $\hat{\boldsymbol{d}}_i$ is the estimation of $\boldsymbol{d}_i$. $\hat{\boldsymbol{d}}_i$ can be updated by the following adaptation law:

$$\dot{\hat{\boldsymbol{d}}}_i = Proj(\boldsymbol{\gamma}_i \boldsymbol{Z}_{i+1}) = \begin{cases} \boldsymbol{0}, & if\ |\hat{\boldsymbol{d}}_i| = \boldsymbol{d}_{iM}\ and\ \hat{\boldsymbol{d}}_i^T(t) \boldsymbol{Z}_{i+1} > 0 \\ \boldsymbol{\gamma}_i \boldsymbol{Z}_{i+1}, & else \end{cases} \tag{25}$$

where $\boldsymbol{\gamma}_i$ is a positive definite diagonal matrix and $\boldsymbol{d}_{iM}$ the upper bound of $\boldsymbol{d}_i$. Eqs.17 and 22 can then be written as:

$$\begin{cases} \boldsymbol{M}_2 \dot{\boldsymbol{Z}}_2 + \boldsymbol{C}_2 \boldsymbol{Z}_2 = \boldsymbol{\mu} \boldsymbol{Z}_3 - \boldsymbol{k}_2 \boldsymbol{Z}_2 + \boldsymbol{\mu} \boldsymbol{F}_{Lds2} - \tilde{\boldsymbol{d}}_1 + \tilde{\boldsymbol{d}}_1^* \\ \theta_2 \dot{\boldsymbol{Z}}_3 = -\boldsymbol{k}_3 \boldsymbol{Z}_3 \frac{1}{\theta_{2\max}} + \boldsymbol{Q}_{Lds2} - \boldsymbol{Y}_Q - \tilde{\boldsymbol{d}}_2 + \tilde{\boldsymbol{d}}_2^* \end{cases} \tag{26}$$

$\boldsymbol{F}_{Lds2}$ and $\boldsymbol{Q}_{Lds2}$ must satisfy the following conditions:

(1) Condition 1

$$\begin{aligned} \boldsymbol{Z}_2^T \boldsymbol{\mu} \boldsymbol{F}_{Lds2} \le 0 \\ \boldsymbol{Z}_3^T \boldsymbol{Q}_{Lds2} \le 0 \end{aligned} \tag{27}$$

(2) Condition 2

$$\begin{aligned} \boldsymbol{Z}_2^T(\boldsymbol{\mu F}_{Lds2}-\tilde{\boldsymbol{d}}_1+\tilde{\boldsymbol{d}}_1^*)\le\eta_1 \\ \boldsymbol{Z}_3^T(\boldsymbol{\mu Q}_{Lds2}-\tilde{\boldsymbol{d}}_2+\tilde{\boldsymbol{d}}_2^*)\le\eta_2 \end{aligned} \tag{28}$$

where η_1 and η_2 are constants. One possible form of $\boldsymbol{F}_{Lds2}$ and $\boldsymbol{Q}_{Lds2}$ can therefore be expressed as:

$$\begin{cases} \boldsymbol{F}_{Lds2}=-\boldsymbol{k}_{2s1}\boldsymbol{Z}_2,\boldsymbol{k}_{2s1}=\dfrac{1}{4\eta_1}(\boldsymbol{d}_{1M}+\|\boldsymbol{\theta}_M\|\|\boldsymbol{\varphi}_{1m}\|+\nu_1)^2 \\ \boldsymbol{Q}_{Lds2}=-\boldsymbol{k}_{2s2}\boldsymbol{Z}_3,\boldsymbol{k}_{2s2}=\dfrac{1}{4\eta_2}(\boldsymbol{d}_{2M}+\|\boldsymbol{\theta}_M\|\|\boldsymbol{\varphi}_{2m}\|+\nu_2)^2 \end{cases} \tag{29}$$

where $\boldsymbol{\theta}_M$ is the upper limit of $\boldsymbol{\theta}$ and $\nu_i(i=1,2)$ are positive definite diagonal matrixes.

By now the design of $\boldsymbol{Q}_{Ld}$ has finished and the valve control voltage U_{vi} can be obtained from Eq. 5.

3.2.Least squares parameter estimation

In the previous steps, $\boldsymbol{Q}_{Ld}$ is designed to replace $\boldsymbol{Q}_L$, and it is enough to ensure basic tracking accuracy. In this part, a least squares parameter estimation law is proposed. Due to the method's characteristics of exponential convergence, high accuracy and fast computational speed, it is suitable for estimating m_t.

The virtual control torque $\boldsymbol{u}_{si}(i=1,2)$ can be expressed as:

$$\begin{aligned} &\boldsymbol{u}_{si}=-\bar{\boldsymbol{\varphi}}_{im}^T\boldsymbol{\theta}_{si},\ i=1,2 \\ &\begin{cases} \bar{\boldsymbol{\varphi}}_{1m}^T=\boldsymbol{\varphi}_1^T \\ \boldsymbol{\theta}_{s1}^T=[\theta_1,\theta_3,\theta_4,\cdots,\theta_{3n+2}] \\ \boldsymbol{u}_{s1}=\boldsymbol{\mu F}_L \end{cases} \\ &\begin{cases} \bar{\boldsymbol{\varphi}}_{2m}^T=[-\dot{\boldsymbol{F}}_L,\boldsymbol{B}_Q,\boldsymbol{C}_Q] \\ \boldsymbol{\theta}_{s2}^T=[\theta_2,\theta_{3n+3},\theta_{3n+4},\cdots,\theta_{5n+2}] \\ \boldsymbol{u}_{s2}=\boldsymbol{Q}_L-\boldsymbol{\mu A}_Q\dot{\boldsymbol{q}} \end{cases} \end{aligned} \tag{30}$$

To eliminate the noise caused by insufficient sensor accuracy, a first-order differential device is designed here. It has the following property.

Property 2

The first-order differential device has the following form:

$$\begin{aligned} &\sigma \dot{x}_f + x_f = x, \quad x(0) = 0 \\ &x_{fnext} = \dot{x}_f t_s + x_f \end{aligned} \tag{31}$$

where x_f is the filtered x, x_{fnext} the updated x_f, σ the time constant selected for first-order differential filtering and t_s the sampling time. It is noteworthy that when the initial condition, denoted as $x(0) \neq 0$, an exponential decay term, represented by $e^{-\frac{t}{\sigma}} x(0) \to 0 \text{ with } t \to \infty$, emerges. The presence of this diminishing term does not substantially influence the principal outcomes of the convergence analysis. Consequently, for the sake of simplicity, the influence of this initial condition will be omitted in the subsequent analysis. After filtering, the first equation in Eq.30 is described as Eq.32 and its estimation error can be expressed as Eq.33.

$$\boldsymbol{u}_{sif} = -\bar{\boldsymbol{\varphi}}_{if}^T \boldsymbol{\theta}_{si}, \; i = 1,2 \tag{32}$$

$$\boldsymbol{\varepsilon}_i = \hat{\boldsymbol{u}}_{sif} - \boldsymbol{u}_{sif} = -\bar{\boldsymbol{\varphi}}_{if}^T \tilde{\boldsymbol{\theta}}_{si}, \quad i = 1,2 \tag{33}$$

The positive definite gain matrix $\Gamma_i (i = 1,2)$ can thus be expressed as:

$$\dot{\Gamma}_i = \begin{cases} \alpha_i \Gamma_i - \zeta_i \Gamma_i \bar{\boldsymbol{\varphi}}_{if} \bar{\boldsymbol{\varphi}}_{if}^T \Gamma_i, & if \; \lambda_{imax}(\Gamma_i(t)) \leq \rho_{iM} \\ 0, & otherwise \end{cases}, i = 1,2 \tag{34}$$

where α_i is the forgetting factor and ρ_{iM} the upper bound of the projective adaptive law, $\zeta_i = (1 + v_i^T \boldsymbol{\varphi}_{if}^T \Gamma_i \boldsymbol{\varphi}_i v_i)^{-1}$, and all the elements in $v_i \in \mathbb{R}^n$ are positive. Then, the projective adaptive law can be written by:

$$\dot{\hat{\boldsymbol{\theta}}}_{si} = Proj_{\hat{\theta}}(\Gamma \tau), \tau = \zeta_i \boldsymbol{\varphi}_{if} \varepsilon_i \tag{35}$$

The projection function that satisfies Eq. 9 should be designed to bound the uncertain parameters. One of the possible choices would be:

$$Proj_{\hat{\theta}}(\bullet)=\begin{cases}\bullet, & if \quad \hat{\boldsymbol{\theta}}\in\partial\overset{o}{\boldsymbol{\Omega}}_{\theta} \ or \ (\boldsymbol{n}_{\hat{\theta}}^{T}\bullet)\le 0\\ (\boldsymbol{I}-\Gamma\dfrac{\boldsymbol{n}_{\hat{\theta}}\boldsymbol{n}_{\hat{\theta}}^{T}}{\boldsymbol{n}_{\hat{\theta}}^{T}\Gamma\boldsymbol{n}_{\hat{\theta}}})\bullet, & if \quad \hat{\boldsymbol{\theta}}\in\partial\boldsymbol{\Omega}_{\theta} \ and \ (\boldsymbol{n}_{\hat{\theta}}^{T}\bullet)>0\end{cases} \tag{36}$$

where $\overset{o}{\boldsymbol{\Omega}}_{\theta}$ and $\boldsymbol{\Omega}_{\theta}$ denote the interior and boundaries of the parameter sets, respectively. $\boldsymbol{n}_{\hat{\theta}}$ is the unit normal vector pointing to the external world when $\hat{\boldsymbol{\theta}}$ is at the boundary.

Eq.36 is used to update m_t. To achieve fast parameter adaptation effect, parameters should be carefully adjusted. It is noteworthy that α_1 should be as small as possible to minimize the impact of older data on new data. Conversely, Γ_1 should be large enough so that the speed of parameter convergence can be maximized.

Due to the frequent changes in unknown load mass under actual working conditions, if the m_t cannot be updated quickly, the control accuracy will be difficult to ensure. Eq.36 indicates how Γ_1 is updated. However, it cannot guarantee that Γ_1 can be large enough to quickly update m_t. When the load of the manipulator changes, it can be considered that the adaptive value of m_t has fallen into local optima. At this time, Γ_1 should be modified to drive the adaptation of m_t and make it jump out of local optima.

The objective function is shown as:

$$\Delta F = F_L - F_{nLda1} \tag{37}$$

where $F_L = p_{1n}A_{1n} - p_{2n}A_{2n}$ and F_{nLda1} is the last item in $\boldsymbol{F}_{Lda1}$. Subsequently, Γ_1 follows the modification law expressed as:

$$\Gamma_1=\begin{cases}\bar{\Gamma}_1, & \Delta F > F_{Max} \text{ or } \Delta F < F_{Min}\\ \Gamma_1, & \text{else}\end{cases} \tag{38}$$

where $\bar{\Gamma}_1$ is the original parameter of Γ_1, F_{Max} and F_{Min} are known functions.

Theorem I

All the signals in the system are bounded. If a positive-definite function is defined as $V_s = \frac{1}{2}\boldsymbol{\omega}_1 \boldsymbol{Z}_2^T \boldsymbol{M}_2 \boldsymbol{Z}_2 + \frac{1}{2}\boldsymbol{\omega}_2 \theta_2 \boldsymbol{Z}_3^T \boldsymbol{Z}_3$, then the following inequality is satisfied:

$$V_s(t) \le \exp(-\lambda t) V_s(0) + \frac{\eta}{\lambda}[1 - \exp(-\lambda t)] \tag{39}$$

where $\lambda = 2 \times \min\{\lambda_{min}(k_2)/k_M, \lambda_{min}(k_3)/\theta^2_{2\max}\}$, $k_M \boldsymbol{I}_n \ge \boldsymbol{M}(q)$.

Theorem II

If the persistent excitation condition is satisfied, $\hat{\boldsymbol{\theta}}$ is able to converge to its real value in the presence of parameter uncertainty only. Based on theorem I, zero angular tracking error can be achieved, i.e., $\boldsymbol{Z}_1 \to 0$ when $t \to \infty$.And the proof of Theorem I and Theorem II can be found in Appendix

Remark I

Theorem I indicates that the controller possesses exponential converging rate. Theorem II demonstrates that uncertain parameters such as m_t can be estimated online and the negative impact of parameter uncertainty can be eliminated through parameter estimation.

4. Simulation

In the simulation, a four-DOF hydraulic manipulator is modeled using MATLAB and Simscape Multibody. The angle coupling, friction and gravity are all taken into consideration. The parameters of the links and hydraulic systems are strictly consistent with the real manipulator. In the simulation, a spherical object with a mass of 10kg and a radius of 0.04m is fixed in the gripper of the manipulator. The distance between the center of the weight and the rotation axis of joint-4 is set to 0.4m. Point-to-point trajectory is used in this experiment, as shown in Fig.3.

The control methods used in the simulation are explained as follows:

C1: PID controller with coefficients being tuned to enhance the tracking accuracy.

C2: DIARC controller with load compensation.

C3: DIARC controller without load compensation. Similar to C2, but the unknown load m_t will not be compensated, i.e. $\theta_1 = 0$. The other parameters are the same as C2.

Fig.4 shows the tracking error of the three methods. The control accuracy using C1 is the lowest, with the maximum error of joint-2 reaching 0.13 rad. C3 can achieve much better performance than PID controller. C2 has the best control accuracy in all four joints, that the max errors decrease by 29.75%, 67.25%, 43.96% and 40.04%, respectively.

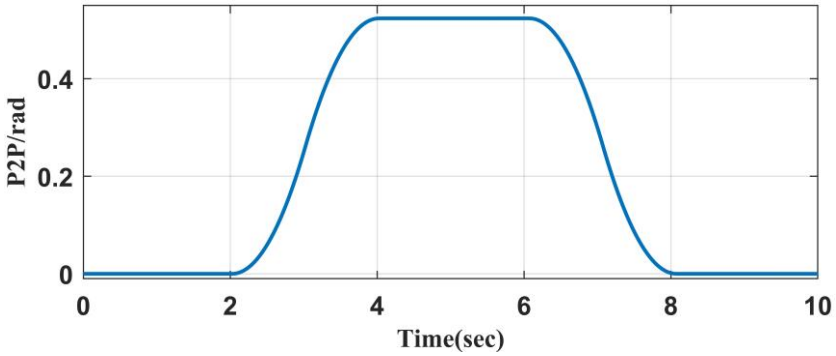

Fig. 3. The trajectory in the experiment and simulation

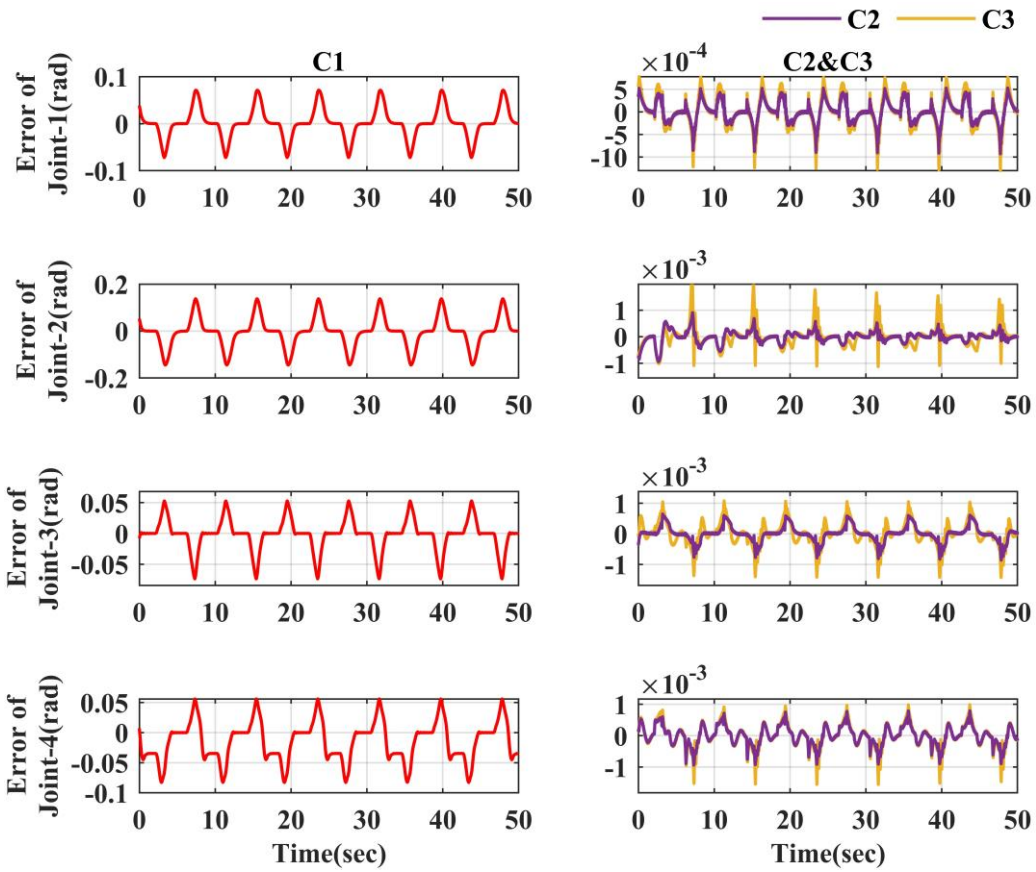

Fig. 4. Simulation results on tracking accuracy

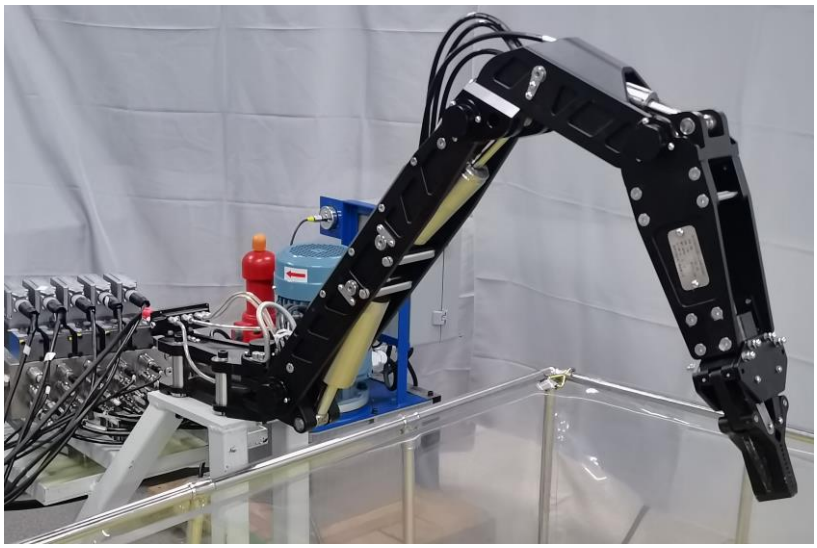

Fig.5. The tested four-DOF manipulator

5. Experiment setup

5.1. Hardware platforms

The tested four-DOF manipulator is shown in Fig.5. The hydraulic system of the

manipulator has the pump driving motor (ABB M2BAX-112MA-4), with rated power being 4KW and maximum output flowrate being 12L/min. It installs two pressure sensors (GEFRAN-KS-E-E-Z-B16D M-V-530) to measure the pressure of each chamber. There are four angle sensors (Melexis-MLX90316) located on each joint. Quarc QPID-e and Q8-USB are utilized to process the data collected by the sensors. The overall sampling time is set to be 25ms.

5.2.Experiment design

To verify the effectiveness of the algorithm for precise motion control and precise load estimation, two sets of experiments were designed as follows:

Set 1: PID trajectory tracking experiment. The end of the manipulator grabs a heavy object with unknown mass, and each joint tracks the P2P trajectory while changing the load mass multiple times to test the effectiveness of the proposed algorithm for precision control and load estimation.

Set 2: Simulation of common handling tasks. The manipulator grabs a heavy object at starting point and transports it to the designated end B, while estimating the mass of the unknown load in real-time.

Using the parameters in simulation as reference, the coefficients in the experiment are set as follows:

Table 1 Coefficients of C2

Coefficients	Value
$\boldsymbol{k}_1$	$[100, 70, 55, 90]^T$
$\boldsymbol{k}_2$	$[75, 35, 45, 70]^T$
$\boldsymbol{k}_3$	$[80, 40, 40, 85]^T$
γ_1	$[220, 280, 150, 120]^T$
γ_2	$[6\times10^{-7}, 8.6\times10^{-7}, 9\times10^{-8}, 3\times10^{-7}]^T$

Table 2 Control performance of each controller

Controller	Angle	Maximum error ($\times 10^{-4}$ deg)	RMSE ($\times 10^{-6}$ deg)	IAE (deg × s)
C1	Joint-1	636	300	1210
	Joint-2	1819	5100	5378
	Joint-3	2067	6800	6350
	Joint-4	1135	1200	2687
C2	Joint-1	77	4.304	201.5
	Joint-2	107	8.358	261.98
	Joint-3	120	7.538	202.56
	Joint-4	99	5.01	194.28
C3	Joint-1	115	8.4	264.89
	Joint-2	151	8.367	279.13
	Joint-3	139	10.97	261.21
	Joint-4	155	18.43	352.47

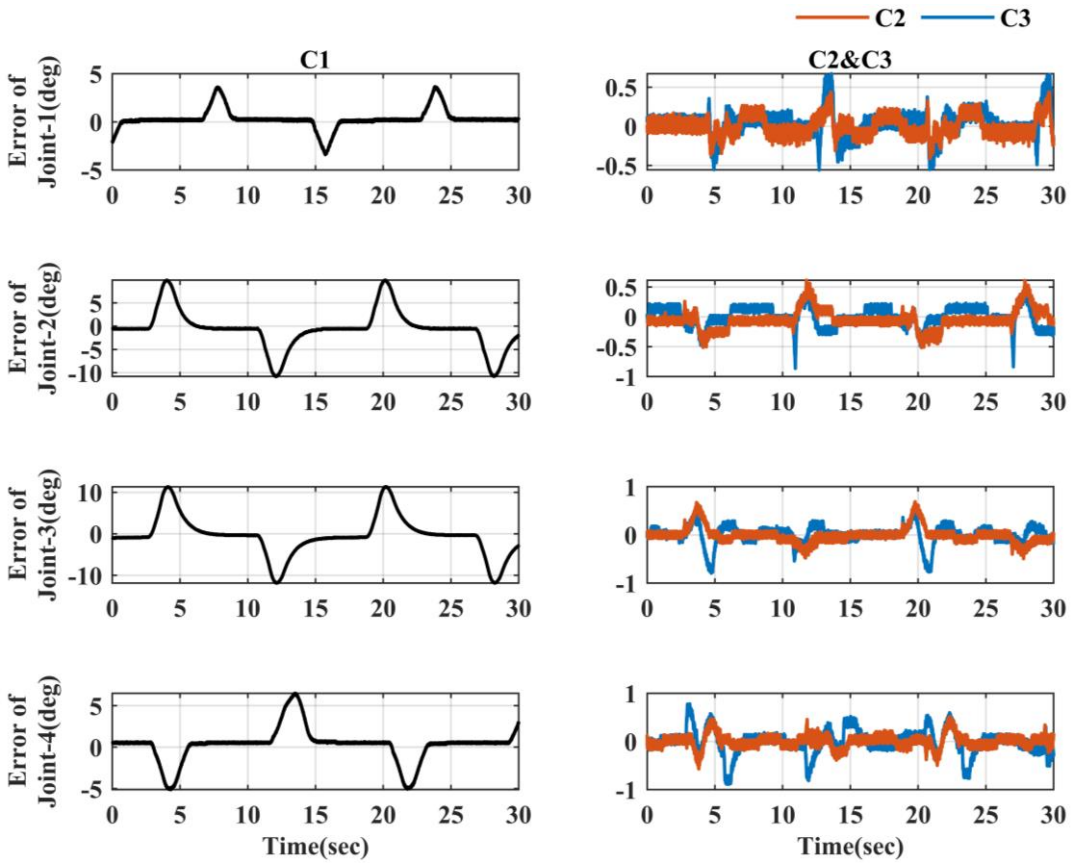

Fig. 6. Experiment results on tracking accuracy

C1: PID controller. The control coefficients are $k_p = [10\ \ 14\ \ 44\ \ 6]$, $k_i = [2\ \ 2.5\ \ 1.5\ \ 4]$, $k_d = [0.5\ \ 0.3\ \ 0.5\ \ 1]$.

C2: DIARC controller with load compensation. The coefficient settings are shown in Table 1. All parameter estimation initial values are set to 0

C3: DIARC controller without load compensation. $\theta_1 = 0$ and other coefficients and the initial values of parameter estimation are the same as C2.

6. Experiment results

Set 1:

Fig.6 shows the tracking performance of each controller. Table 2 lists the maximum tracking error, root mean squared error (RMSE) and integral absolute error (IAE). It can be seen that C1 is far inferior in control accuracy to C2 and C3 because the complex dynamics of the hydraulic manipulator is considered. For DIARC controllers, load compensation also has a significant effect. In C2, the control accuracy of joint-2, joint-3 and joint-4 which is directly affected by the unknown load mass has greatly improved. Compared to C3, the maximum errors of the joints decrease by 29.14%, 13.67% and 36.13%, respectively. Due to the high estimation accuracy of the unknown load mass, the maximum error of the joint-1 also reduces by 33.04%. RMSE and IAE of all joints

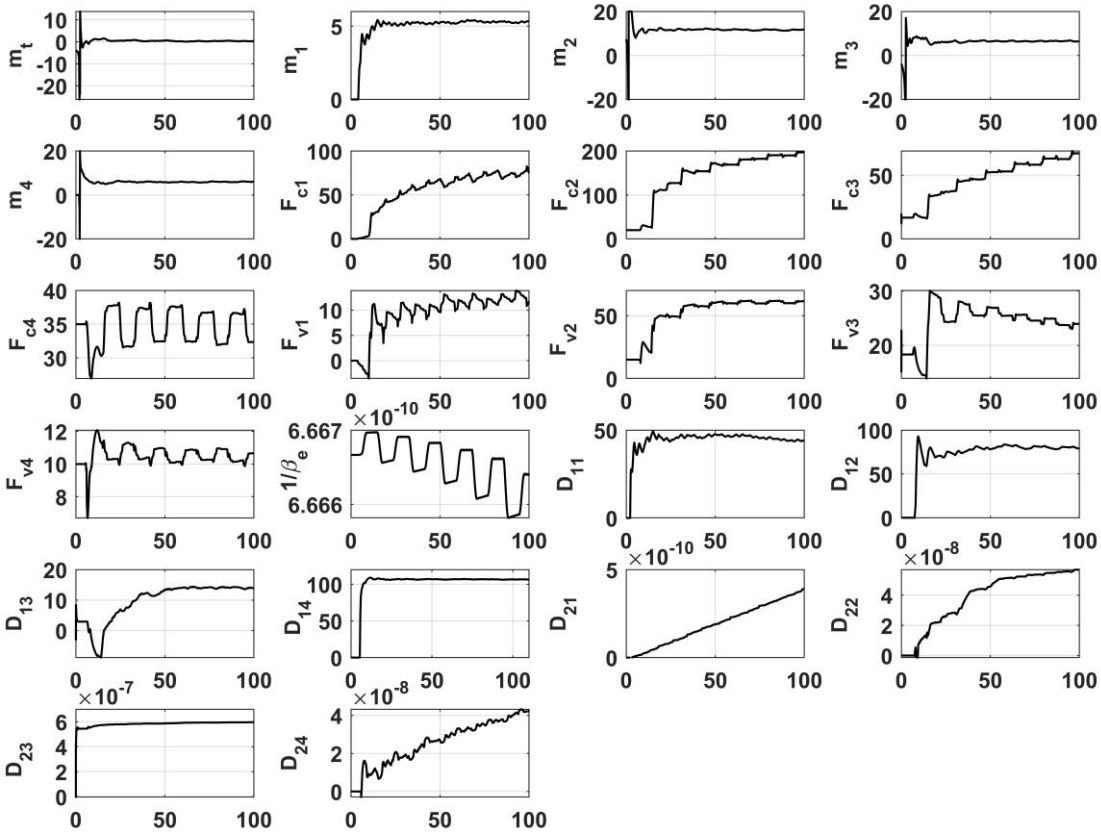

Fig. 7. Adaptive curves of all parameters

also decrease evidently.

For C2, accurate parameter estimation is an important feature. The adaptive curves of all parameters of the controller are shown in Fig.7. It demonstrates that each parameter converges to a certain value and the convergence value is largely trustworthy.

Additionally, the manipulator is operated under no-load, loads of 2.5kg, 5kg, and 7.5kg respectively. For each unknown load mass (including no-load), the manipulator runs repeatedly and collect ten sets of data. The average, maximum, and minimum values, RMSE and standard deviation (SD) list in table 3.

From the experimental data, the average estimation error is always below 5%, and the maximum error does not exceed 10%. Although the estimated values of mass witness certain fluctuation, with the maximum difference reaching 0.79kg, the average estimated value is close to the actual value. It depicts that the developed controller has an ability to achieve estimation accuracy.

In practical engineering, the unknown load mass of a manipulator is often time-varying. Two scenarios are set up to test the controller's real-time estimation of changing loads. In scenario-1, the unknown load mass continues to increase by 0kg, 2.5kg, 5kg, and 7.5kg, respectively. In scenario-2, the unknown load mass switches between 0kg and 2.5kg. The adaptive curves are shown in Fig.8.

Evidently, in both scenarios, the adaptive curve converges to the actual values. In the adaptive curve of scenario-1, the intermediate transition state is marked with backup color. During this period, the load is changed and Γ_1 modification (expressed in Eq. 38) is performed, which is indicated by a spike of the adaptive curve. The duration of this transition state is short, and the parameters will continue to converge to the true value afterwards. The time interval for estimation is short with 10-15s on average and the average estimation error in the experiment is 3.89%.

Table 3 Statistic data in load estimation accuracy

Mass kg	Avg. kg	Max. kg	Min. kg	RMSE kg	SD kg	Error (%) (Avg./Max./Min.)
0	0.175	0.35	-0.1	0.018	0.142	
2.5	2.607	2.74	2.42	0.015	0.127	4.3/9.6/3.2
5	5.14	5.33	4.80	0.062	0.263	2.8/6.6/4.0
7.5	7.71	8.12	7.33	0.055	0.247	2.8/8.3/2.3

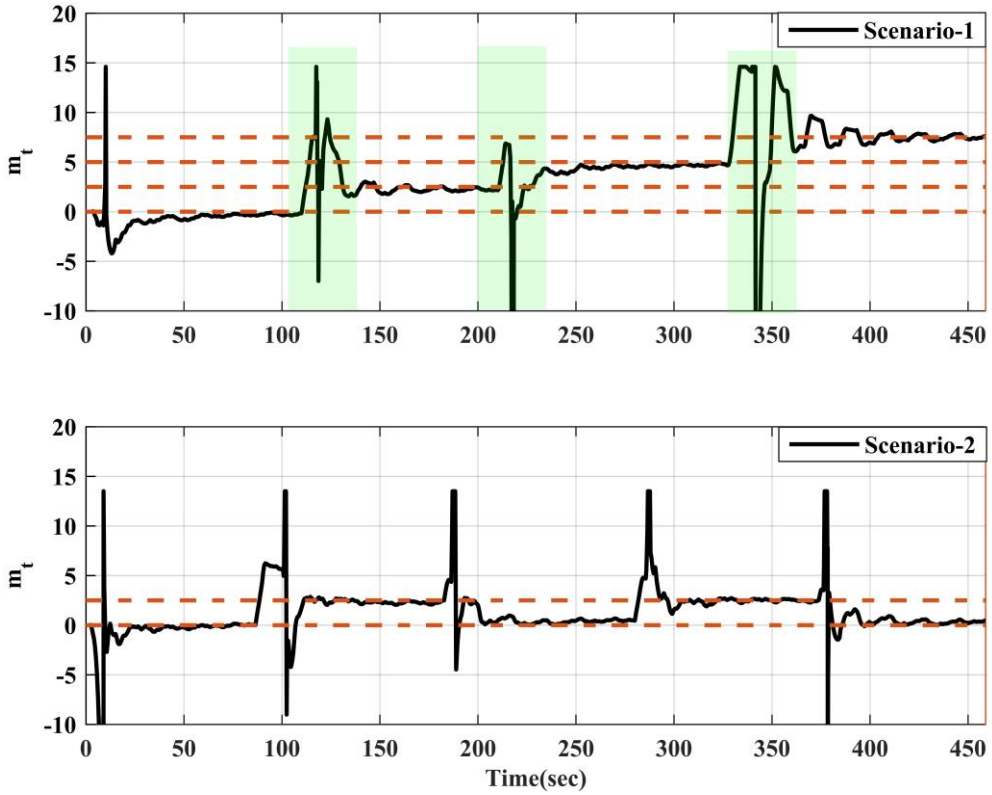

Fig. 8. Adaptive curves with unknown load

Set 2:

In this experiment, a common handling task is performed. The manipulator will carry a weight of 2.5kg and 5kg respectively. The trajectory in joint space and Cartesian space is shown in Figure 9. The tracking results in joint space are shown in Fig. 10. The maximum tracking error occurs at around 9s when the angular velocity witnesses a significant change. But this transient error does not exceed 0.7 degree, and in most cases, the error is limited to within 0.2 degree. Additionally, the tracking results in three dimensions of the Cartesian space are manifested in Fig. 11. Generally, the error in all

directions can be stabilized within 0.5cm, and the maximum error is limited to within 1cm. Meanwhile, it is noted that when the load mass changes from 2.5kg to 5kg, there is no significant change in maximum error and dynamic error, indicating that the compensation for the load mass is effective. To conclude, the designed controller can compensate for unknown load mass and achieve high control accuracy.

The adaptive curves for the two handling tasks are illustrated in Figure 12. The system feels the heavy object being picked up at the beginning and activates the modification of Γ_1, which results in the spike of the curve. At 10s, the curved become relatively stable and gradually converge to the actual values, and it takes around 40 seconds to truly converge to the actual value. In this experiment, the frequency width of velocity

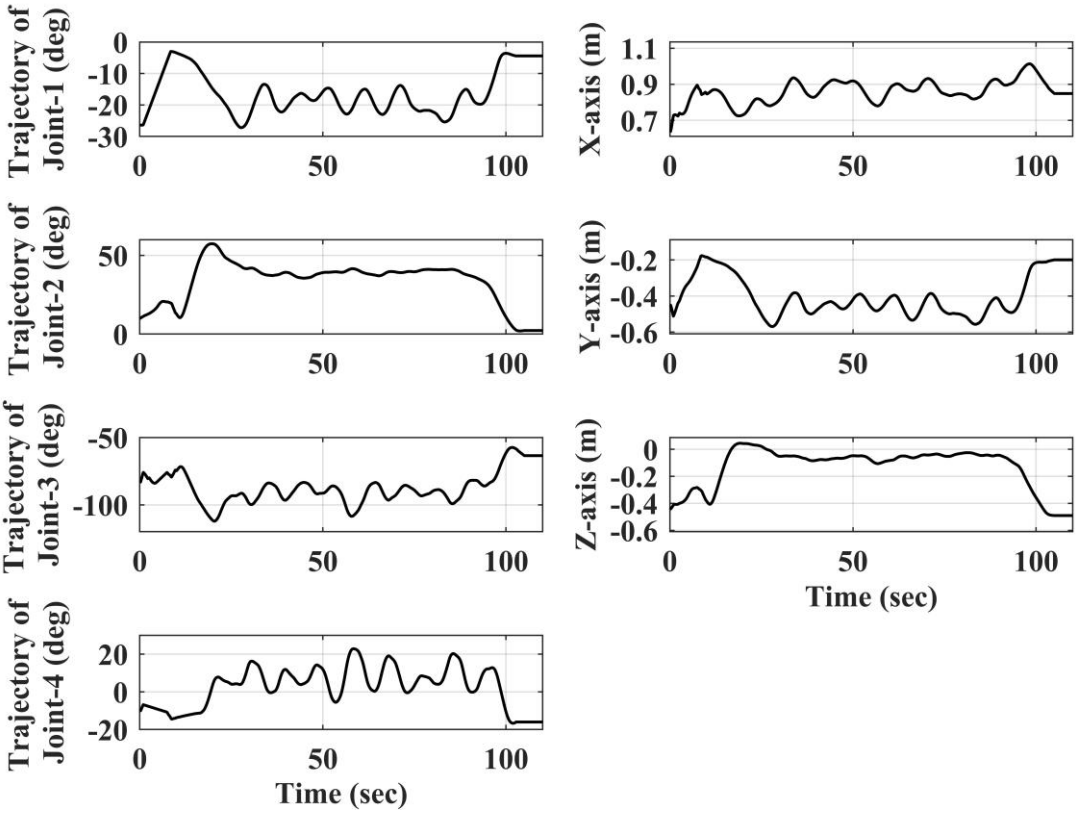

Fig. 9. Desired trajectory of Set-2

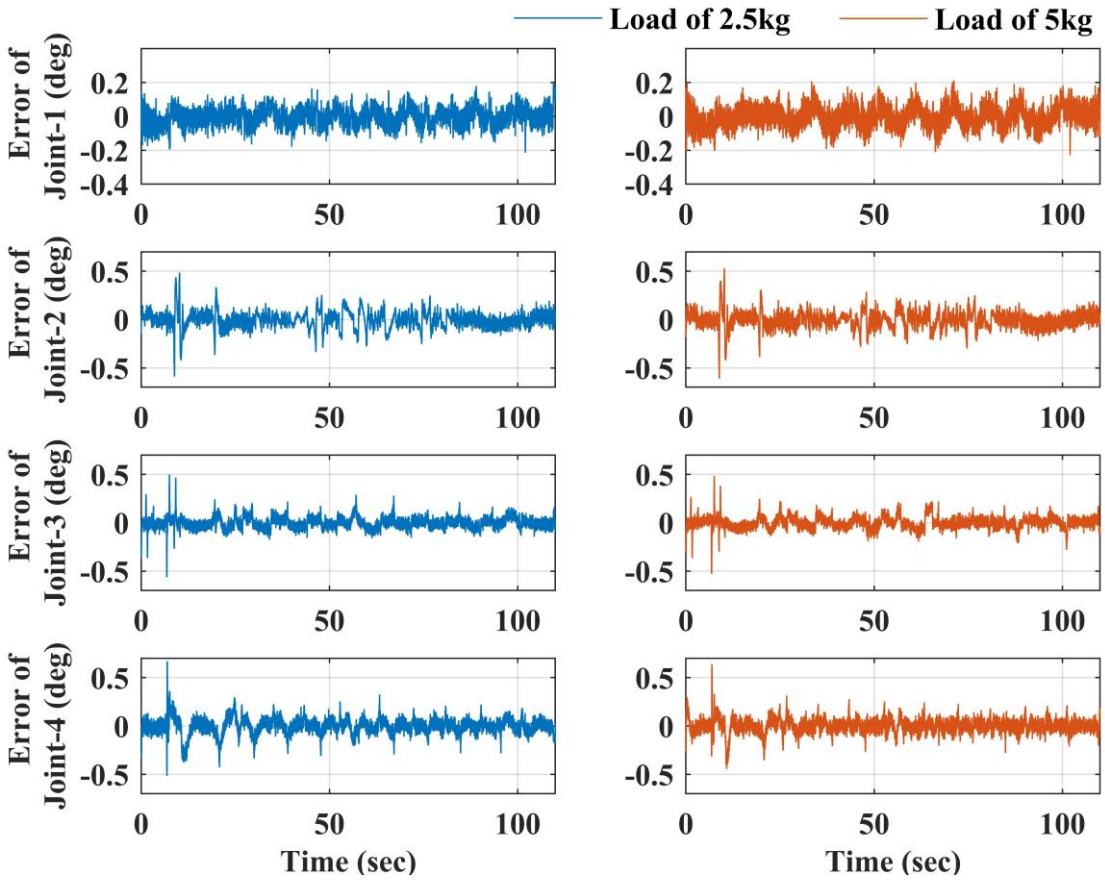

Fig. 10. Tracking performance in joint space

and acceleration is relatively limited, so it is not possible to fully stimulate the dynamic characteristics of the system. Due to the strong correlation between load mass and system velocity and acceleration, the estimation speed of mass is slowed down, but high estimation accuracy is still achieved. A mass of 2.35kg is estimated when the actual weight is 2.5kg, and a mass of 5.22kg is estimated when the actual weight is 5kg. The estimation error is 6% and 4.4%, respectively.

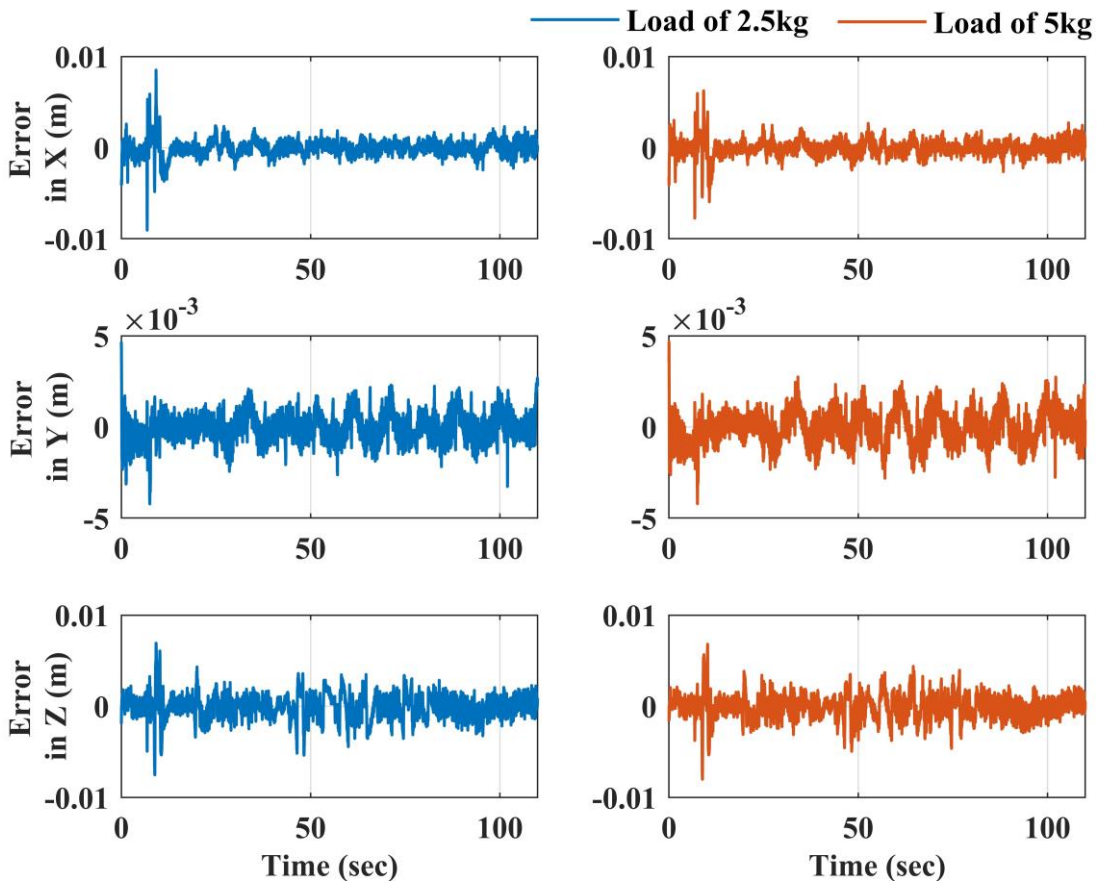

Fig. 11. Tracking performance in Cartesian space

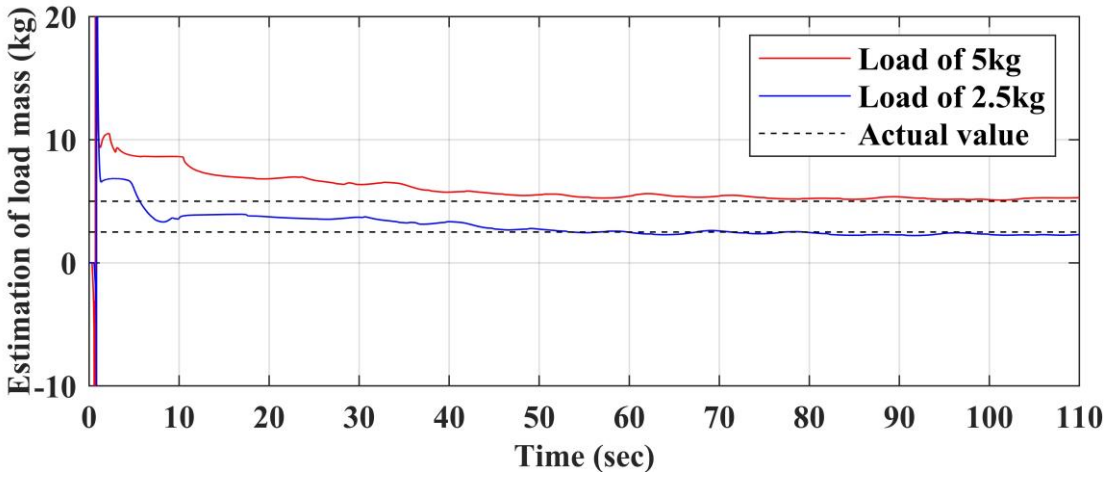

Fig. 12. Adaptive curves in handling tasks

7. Conclusions

This article proposes a direct/indirect adaptive robust controller (DIARC), which can compensate for the influence of the unknown load mass on hydraulic manipulators and can effectively estimate the mass of the unknown load mass. The high-order

dynamics of the hydraulic manipulator with complex nonlinearity can be solved by adopting backstepping strategy which enables the controller to achieve high tracking accuracy. The unknown load mass is modeled and is included in the parametric space, a parameter adaptive law based on least squares method is designed in response to the demand for identification of unknown load mass, and the precise estimation of unknown load mass can be ensured. With the accurate estimation of the unknown load mass, the control accuracy can be further improved. Further research is being conducted to explore enhanced parameter adaptation laws, aimed at enabling quicker and more precise load estimation effects. Additionally, experiments in more challenging conditions, including underwater environments are underway.

The control performance is experimentally verified on a four-DOF hydraulic manipulator. The experimental results show that the proposed controller with unknown load mass compensation reduces steady-state error and dynamic tracking error to a large extent. The accuracy of mass estimation is also relatively high. Overall, the controller can achieve load estimation without the need for pressure sensors, making it suitable for hydraulic manipulators under actual operating conditions. This study has considerable value for mining machinery, sorting machinery, hanging machinery and other industries that calls for precision control and load recognition.

Declaration

Availability of data and materials: All data generated or analysed during this study are included in this published article.

Competing interests: The authors declare that they have no competing interests.

Funding: This work is supported by National Natural Science Foundation of China (No.523B1002 and No.52075476), and Natural Science Foundation of Zhejiang

Province (No. LR23E050001), and Fundamental Research Funds for the Central Universities (226-2023-00029).

Contribution: QW proposed the methodology and conducted experiments, he also drafted the original draft. MQ helped with experiments and utilized software for simulation, he also did investigation on the utilized method. YX helped to organize experiments and conducted data curation. SZ supervised the experiments and helped to polish the paper. ZC supervised the entire research process and offered resources, he is also the administrator of the project and related funding.

Acknowledgement: Not applicable.

Renferences:

1. L. Fang, T. Wang, W. Zheng, Z. Liu, L. Ming, X. Zheng, M. Wu. (2023). Consistency optimal coordination control of underground heavy-load robot in nonstructural environment. Robotics and Autonomous Systems, 159, Article 104281.
   https://doi.org/10.1016/j.robot.2022.104281.
2. R. Capocci, G. Dooly, E. Omerdić, J. Coleman, T. Newe, D. Toal. (2017). Inspection-class remotely operated vehicles—a review. Journal of Marine Science and Engineering, 5(1).
   https://doi.org/10.3390/jmse5010013.
3. L. Lyu, Z. Chen and B. Yao. (2021). Advanced valves and pump coordinated hydraulic control design to simultaneously achieve high accuracy and high efficiency. IEEE Transactions on Control Systems Technology, 29(1), 236-248.
   https://doi.org/10.1109/TCST.2020.2974180.
4. Z. Chen, F. Huang, W. Chen, J. Zhang, W. Sun, J. Chen, J. Gu and S. Zhu. (2020). RBFNN-based adaptive sliding mode control design for delayed nonlinear

multilateral tele-robotic system with cooperative manipulation. IEEE Transactions on Industrial Informatics, 16(2), 1236-1247.
https://doi.org/10.1109/TII.2019.2927806

5. J. Mattila, J. Koivumäki, D. G. Caldwell and C. Semini. (2017). A Survey on Control of Hydraulic Robotic Manipulators With Projection to Future Trends. IEEE/ASME Transactions on Mechatronics, 22(2), 669-680.
https://doi.org/10.1109/TMECH.2017.2668604.
6. J. Hu, C. Li, Z. Chen, B. Yao. (2020). Precision motion control of a 6-dofs industrial robot with accurate payload estimation. IEEE/ASME Transactions on Mechatronics, 25(4), 1821–1829.
https://www.doi.org/10.1109/TMECH.2020.2994231.
7. N. Adhikary, C. Mahanta. (2013). Integral backstepping sliding mode control for underactuated systems: Swing-up and stabilization of the Cart–Pendulum System. ISA Transactions, 52(6), 870-880.
https://doi.org/10.1016/j.isatra.2013.07.012.
8. Y. Yuan and W. Sun. (2023). An integrated kinematic calibration and dynamic identification method with only static measurements for serial robot. IEEE/ASME Transactions on Mechatronics.
https://doi.org/10.1109/TMECH.2023.3241302.
9. R. Ding, M. Cheng, L. Jiang and G. Hu. (2021). Active fault-tolerant control for electro-hydraulic systems with an independent metering valve against valve faults. IEEE Transactions on Industrial Electronics, 68(8), 7221-7232.
https://doi.org/10.1109/TIE.2020.3001808.

10. J. Yao, W. Deng, Z. Jiao. (2017). RISE-based adaptive control of hydraulic systems with asymptotic tracking. IEEE Transactions on Automation Science and Engineering, 14(3), 1524-1531. https://www.doi.org/10.1109/TIE.2017.2694382.
11. Q. Guo and D. Jiang. (2012). Based on rehabilitation robots of motion control pid research. 2012 International Conference on Control Engineering and Communication Technology, 394-397. https://doi.org/10.1109/ICCECT.2012.110.
12. M. Cheng, J. Zhang, B. Xu, R. Ding and J. Wei. (2018). Decoupling compensation for damping improvement of the electrohydraulic control system with multiple actuators. IEEE/ASME Transactions on Mechatronics, 23(3), 1383-1392. https://doi.org/10.1109/TMECH.2018.2834936.
13. W. Shen, J. Wang. (2022). An integral terminal sliding mode control scheme for speed control system using a double-variable hydraulic transformer. ISA Transactions, 124, 386-394. https://doi.org/10.1016/j.isatra.2019.08.068.
14. B. Yao, F. Bu, J. Reedy and G. T. C. Chiu. (1999). Adaptive robust motion control of single-rod hydraulic actuators: Theory and experiments. Proceedings of the 1999 American Control Conference, 759-763. https://www.doi.org/10.1109/ACC.1999.783142.
15. Y. Xia, Y. Nie, Z. Chen. (2022). Motion control of a hydraulic manipulator with adaptive nonlinear model compensation and comparative experiments. Machines, 10(3), 214. https://www.doi.org/10.3390/machines10030214.

16. S. Zhou, C. Shen, Y. Xia, Z. Chen, and S. Zhu, “Adaptive robust control design for underwater multi-dof hydraulic manipulator,” Ocean Engineering, 248, Article 110822.
https://doi.org/10.1016/j.oceaneng.2022.110822.
17. Z. Chen, B. Helian, Y. Zhou and M. Geimer. (2023). An integrated trajectory planning and motion control strategy of a variable rotational speed pump-controlled electro-hydraulic actuator. IEEE/ASME Transactions on Mechatronics, 28(1), 588-597.
https://doi.org/10.1109/TMECH.2022.3209873.
18. X. Yang, J. Yao, W. Deng, S. Yuan and X. Liang. (2021). Asymptotic adaptive motion control of hydraulic systems. 2021 40th Chinese Control Conference (CCC), 302-307.
https://doi.org/10.23919/CCC52363.2021.9549358.
19. L. Yin, J. Yao and Z. Yao. (2020). Finite frequency H∞ control for electro-hydraulic servo system with parameter uncertainties. 2020 5th International Conference on Advanced Robotics and Mechatronics (ICARM), 477-482.
https://doi.org/10.1109/ICARM49381.2020.9195399.
20. Z. Xu, L. Li, J. Yao, X. Hu, Q. Liu and N. Xie. (2019). State constraint control for uncertain nonlinear systems with disturbance compensation. IEEE Access, 7, 155251-155261.
https://doi.org/10.1109/ACCESS.2019.2947629.
21. Z. Yao, J. Yao and W. Sun. (2019). Adaptive RISE control of hydraulic systems with multilayer neural-networks. IEEE Transactions on Industrial Electronics, 66(11), 8638-8647.
https://doi.org/10.1109/TIE.2018.2886773.

22. J. Hou, D. Zhao and D. Ding. (2020). Forcefree control for hydraulic stewart manipulator. 2020 IEEE 9th Joint International Information Technology and Artificial Intelligence Conference (ITAIC), 89-92. https://doi.org/10.1109/ITAIC49862.2020.9338984.
23. S. Chen, Z. Chen, B. Yao, X. Zhu, S. Zhu, Q. Wang, Y. Song. (2017). Adaptive robust cascade force control of 1-DOF hydraulic exoskeleton for human performance augmentation. IEEE/ASME Transactions on Mechatronics, 22(2), 589-600. https://doi.org/10.1109/TMECH.2016.2614987.
24. J. Koivumäki and J. Mattila. (2013). The automation of multi degree of freedom hydraulic crane by using virtual decomposition control. 2013 IEEE/ASME International Conference on Advanced Intelligent Mechatronics, 912-919. https://doi.org/10.1109/AIM.2013.6584210.
25. J. Koivumäki, J. Mattila. (2015). Stability-guaranteed force-sensorless contact force/motion control of heavy-duty hydraulic manipulators. IEEE Transactions on Robotics, 31(4), 918–935. https://doi.org/10.1109/TRO.2015.2441492.
26. G. R. Petrović and J. Mattila. (2022). Mathematical modelling and virtual decomposition control of heavy-duty parallel–serial hydraulic manipulators. Mechanism and Machine Theory, 170, Article 104680. https://doi.org/10.1016/j.mechmachtheory.2021.104680.
27. T. X. Dinh, T. D. Thien, T. H. V. Anh and K. K. Ahn. (2018). Disturbance observer based finite time trajectory tracking control for a 3 DOF hydraulic manipulator including actuator dynamics. IEEE Access, 6, 36798-36809. doi: 10.1109/ACCESS.2018.2848240.

28. T. Lin, Y. Lin, H. Ren, H. Chen, Z. Li, Q. Chen. (2021). A double variable control load sensing system for electric hydraulic excavator. Energy, 223, Article 119999. https://doi.org/10.1016/j.energy.2021.119999.
29. S. Duan, L. Chen, Z. Ma, G. Lu. (2010). Variable structure control with feedforward compensator for robot manipulators subject to load uncertainties. 2010 11th International Conference on Control Automation Robotics & Vision, 2367-2372. https://doi.org/10.1109/ICARCV.2010.5707248.
30. W. Sun, Y. Yuan. (2023). Passivity based hierarchical multi-task tracking control for redundant manipulators with uncertainties, Automatica, 155, Article 111159. https://doi.org/10.1016/j.automatica.2023.111159.
31. A. Zeng, S. Song, J. Lee, A. Rodriguez, T. Funkhouser. (2020). TossingBot: Learning to throw arbitrary objects with residual physics. IEEE Transactions on Robotics, 36(4), 1307-1319. https://doi.org/10.1109/TRO.2020.2988642.
32. A. Colomé, D. Pardo, G. Alenyà, C. Torras. (2013). External force estimation during compliant robot manipulation. In 2013 IEEE International Conference on Robotics and Automation, 3535-3540. https://doi.org/10.1109/ICRA.2013.6631072.
33. H. L. Bartlett, B. E. Lawson and M. Goldfarb. (2019). Design, control, and preliminary assessment of a multifunctional semipowered ankle prosthesis. IEEE/ASME Transactions on Mechatronics, 24(4), 1532-1540. https://doi.org/10.1109/TMECH.2019.2918685.
34. F. Tessari, R. Galluzzi, A. Tonoli, N. Amati, G. Milandri, M. Laffranchi, L. De Michieli. (2020). An integrated, back-drivable electro-hydrostatic actuator for a

knee prosthesis. In 2020 8th IEEE RAS/EMBS International Conference for Biomedical Robotics and Biomechatronics (BioRob), 708-714. https://doi.org/10.1109/BioRob49111.2020.9224278.

35. A. Renner, H. Wind, O. Sawodny. (2020). Online payload estimation for hydraulically actuated manipulators. Mechatronics, 66, Article 102322. https://doi.org/10.1016/j.mechatronics.2020.102322.
36. A. Mohanty, B. Yao. (2011). Integrated direct/indirect adaptive robust control of hydraulic manipulators with valve deadband. IEEE/ASME Transactions on Mechatronics, 16(4), 707-715. https://doi.org/10.1109/TMECH.2010.2051037.
37. G.C. Goodwin, D.Q. Mayne. (1987). A parameter estimation perspective of continuous time model reference adaptive control. Automatica, 23(1), 57-70. https://doi.org/10.1016/0005-1098(87)90118-X.

Appendix A

Detailed expression of $\boldsymbol{M}_t$, $\boldsymbol{C}_t$ and $\boldsymbol{G}_t$:

$$\boldsymbol{M}_t = \begin{pmatrix} M_{11} & 0 & 0 & 0 \\ 0 & M_{22} & M_{23} & M_{24} \\ 0 & M_{32} & M_{33} & M_{34} \\ 0 & M_{42} & M_{43} & M_{44} \end{pmatrix},\ \boldsymbol{C}_t = \begin{pmatrix} C_{11} & C_{12} & C_{13} & C_{14} \\ C_{21} & C_{22} & C_{23} & C_{24} \\ C_{31} & C_{32} & C_{33} & C_{34} \\ C_{41} & C_{42} & C_{43} & 0 \end{pmatrix},\ \boldsymbol{G}_t = \begin{pmatrix} 0 \\ G_2 \\ G_3 \\ G_4 \end{pmatrix}$$

$M_{11} = (L_1 + L_3C_{23} + L_2C_2 + L_4C_{234})^2,\ M_{22} = M_{33} + L_2^2 + 2(C_2L_2L_3 + C_{34}L_2L_4)$

$M_{23} = M_{32} = M_{33} + (2C_{23}L_2L_4 + C_3L_2L_3),\ M_{24} = M_{42} = M_{34} + L_4L_2C_{34}$

$M_{33} = M_7 + (L_3^2 + 2C_4L_3L_4),\ M_{34} = M_{43} = L_4(L_3C_4 + L_4),\ M_{44} = L_4^2$

$x = (L_1 + L_2C_2 + L_3C_{23} + L_4C_{234}),\ C_{11} = -(x - L_1)(\dot{\alpha}_2 + \dot{\alpha}_3 + \dot{\alpha}_4)x$

$C_{12} = -L_2\dot{\alpha}_1S_2x + C_{13}, C_{13} = -L_3\dot{\alpha}_1S_{23}x + C_{14},\ C_{14} = -L_4\dot{\alpha}_1S_{234}x$

$C_{21} = L_2S_2\dot{\alpha}_1x + C_{31},\ C_{22} = -\dot{\alpha}_3(L_2L_4S_{34} + L_2L_3S_3) - \dot{\alpha}_4(L_2L_4S_{34} + L_3L_4S_4)$

$C_{23} = -(\dot{\alpha}_2 + \dot{\alpha}_3 + \dot{\alpha}_4)L_2L_4S_{34} - (\dot{\alpha}_2 + \dot{\alpha}_3)L_2L_3S_3 + C_{33},\ C_{24} = C_{34} - L_2L_4S_{34}(\dot{\alpha}_2 + \dot{\alpha}_3 + \dot{\alpha}_4)$

$C_{31} = L_3S_{23}\dot{\alpha}_1x + C_{41},\ C_{32} = L_2L_4S_{34}\dot{\alpha}_2 + L_2L_3S_3\dot{\alpha}_2 + C_{33},\ C_{33} = -L_3L_4S_4\dot{\alpha}_4,\ C_{34} = C_{33} - C_{43}$

$C_{41} = L_4S_{234}\dot{\alpha}_1x,\ C_{42} = L_2L_4S_{34}\dot{\alpha}_2 + C_{43},\ C_{43} = L_3L_4S_4(\dot{\alpha}_2 + \dot{\alpha}_3)$

$G_2 = gL_2C_2 + G_3,\ G_3 = gL_3C_{23} + G_4,\ G_4 = gL_4C_{234}$

Appendix B

Proof for theorem I

The Lyapunov function is defined as:

$$V_s = \frac{1}{2}\boldsymbol{\omega}_1 \boldsymbol{Z}_2^T \boldsymbol{M}_2 \boldsymbol{Z}_2 + \frac{1}{2}\boldsymbol{\omega}_2 \theta_2 \boldsymbol{Z}_3^T \boldsymbol{Z}_3 \tag{40}$$

Since $\dot{\boldsymbol{M}}_2 = \boldsymbol{C}_2 + \boldsymbol{C}_2^T$, the derivative of Eq. 40 can be written as:

$$\begin{aligned} \dot{V}_s &= \boldsymbol{\omega}_1 \boldsymbol{Z}_2^T (\boldsymbol{M}_2 \dot{\boldsymbol{Z}}_2 + \boldsymbol{C}_2 \boldsymbol{Z}_2) + \boldsymbol{\omega}_2 \theta_2 \boldsymbol{Z}_3^T \dot{\boldsymbol{Z}}_3 \\ &= \boldsymbol{\omega}_1 \boldsymbol{Z}_2^T (-\boldsymbol{\varphi}_{1m}^T \boldsymbol{\theta} + \boldsymbol{\mu} \boldsymbol{F}_L + \Delta \boldsymbol{D}_1) + \boldsymbol{\omega}_2 \boldsymbol{Z}_3^T (-\boldsymbol{A}_Q \boldsymbol{\mu} \dot{\boldsymbol{\alpha}} + \boldsymbol{Q}_L + \boldsymbol{\varphi}_{2m}^T \boldsymbol{\theta} + \Delta \boldsymbol{D}_2) \end{aligned} \tag{41}$$

Considering Eqs. 15 and 21, Eq. 41 can be expressed as:

$$\begin{aligned} \dot{V}_s = &-\boldsymbol{\omega}_1 \boldsymbol{Z}_2^T \boldsymbol{k}_2 \boldsymbol{Z}_2 + \boldsymbol{\omega}_1 \boldsymbol{Z}_2^T (\mu \boldsymbol{Z}_3 - \tilde{\boldsymbol{d}}_1 + \tilde{\boldsymbol{d}}_1^* + \boldsymbol{\mu} \boldsymbol{F}_{Lds2}) \\ &-\boldsymbol{\omega}_2 \frac{\boldsymbol{k}_3}{\theta_{2\max}} \boldsymbol{Z}_3^T + \boldsymbol{\omega}_2 \boldsymbol{Z}_3^T (\boldsymbol{Y}_Q - \tilde{\boldsymbol{d}}_2 + \tilde{\boldsymbol{d}}_2^* + \boldsymbol{Q}_{Lds2}) \end{aligned} \tag{42}$$

Noting Eq. 29 and $\boldsymbol{Y}_Q = -\boldsymbol{\mu} \boldsymbol{Z}_2 \frac{\boldsymbol{\omega}_1}{\boldsymbol{\omega}_2}$, Eq. 42 can be expressed as:

$$\begin{aligned} \dot{V}_s &\le -\boldsymbol{\omega}_1 \boldsymbol{Z}_2^T \boldsymbol{k}_2 \boldsymbol{Z}_2 - \boldsymbol{\omega}_2 \frac{\boldsymbol{k}_3}{\theta_{2max}} \boldsymbol{Z}_3^T + \boldsymbol{\omega}_1 \eta_1 + \boldsymbol{\omega}_2 \eta_2 \\ &\le -\lambda V_s + \eta \end{aligned} \tag{43}$$

Then apply the comparison theorem, we can get:

$$V_s(t) \le \exp(-\lambda t) V_s(0) + \frac{\eta}{\lambda}[1 - \exp(-\lambda t)] \tag{44}$$

The boundedness of the closed-loop system signal is guaranteed. The relation between the Laplace transform of $\boldsymbol{Z}_1$ and $\boldsymbol{Z}_2$ can be written as:

$$\frac{\boldsymbol{Z}_1(s)}{\boldsymbol{Z}_2(s)} = \frac{1}{1 + \boldsymbol{k}_1 s} \tag{45}$$

Therefore, if $\boldsymbol{Z}_2$ is bounded, $\boldsymbol{Z}_1$ will be bounded as well.

Appendix C

Proof for theorem II

According to Ref [37], when $\Delta \boldsymbol{D}_1 = \Delta \boldsymbol{D}_2 = 0$ and PE condition is fulfilled, $\tilde{\boldsymbol{\theta}} \to 0$ when $t \to 0$. The Lyapunov function can be defined as:

$$V_a = V_s + \frac{1}{2}\boldsymbol{\omega}_1 \hat{\boldsymbol{d}}_1^T \Gamma_1 \hat{\boldsymbol{d}}_1 + \frac{1}{2}\boldsymbol{\omega}_2 \hat{\boldsymbol{d}}_2^T \Gamma_2 \hat{\boldsymbol{d}}_2 \tag{46}$$

The derivative of Eq. 46 can be written as:

$$\begin{aligned} \dot{V}_a &= \boldsymbol{\omega}_1 \boldsymbol{Z}_2^T (\boldsymbol{M}_2 \dot{\boldsymbol{Z}}_2 + \boldsymbol{C}_2 \boldsymbol{Z}_2) + \boldsymbol{\omega}_2 \theta_2 \boldsymbol{Z}_3^T \dot{\boldsymbol{Z}}_3 + \boldsymbol{\omega}_1 \hat{\boldsymbol{d}}_1^T \Gamma_1 \dot{\hat{\boldsymbol{d}}}_1 + \boldsymbol{\omega}_2 \hat{\boldsymbol{d}}_2^T \Gamma_2 \dot{\hat{\boldsymbol{d}}}_2 \\ &= \boldsymbol{\omega}_1 \boldsymbol{Z}_2^T (\boldsymbol{M}_2 \dot{\boldsymbol{Z}}_2 + \boldsymbol{C}_2 \boldsymbol{Z}_2) + \boldsymbol{\omega}_2 \theta_2 \boldsymbol{Z}_3^T \dot{\boldsymbol{Z}}_3 \\ &\quad + \boldsymbol{\omega}_1 \hat{\boldsymbol{d}}_1^T \Gamma_1 (Proj(\boldsymbol{\gamma}_i \boldsymbol{Z}_2) - \boldsymbol{Z}_2) + \boldsymbol{\omega}_2 \hat{\boldsymbol{d}}_2^T \Gamma_2 (Proj(\boldsymbol{\gamma}_i \boldsymbol{Z}_3) - \boldsymbol{Z}_3) \\ &\le -\boldsymbol{\omega}_1 \boldsymbol{Z}_2^T \boldsymbol{k}_2 \boldsymbol{Z}_2 - \boldsymbol{\omega}_2 \frac{\boldsymbol{k}_3}{\theta_{2\max}} \boldsymbol{Z}_3^T + \boldsymbol{\omega}_1 \boldsymbol{Z}_2 \boldsymbol{\varphi}_{1m}^T \tilde{\boldsymbol{\theta}} + \boldsymbol{\omega}_2 \boldsymbol{Z}_3 \boldsymbol{\varphi}_{2m}^T \tilde{\boldsymbol{\theta}} \end{aligned} \tag{47}$$

Since $\tilde{\boldsymbol{\theta}} \in L_2[0,\infty)$ and both $\boldsymbol{\varphi}_{1m}^T$ and $\boldsymbol{\varphi}_{2m}^T$ are bounded, $\boldsymbol{\varphi}_{1m}^T \tilde{\boldsymbol{\theta}} \in L_2[0,\infty)$ and $\boldsymbol{\varphi}_{2m}^T \tilde{\boldsymbol{\theta}} \in L_2[0,\infty)$. From Eq. 47, we can get $\boldsymbol{Z}_2 \in L_2[0,\infty)$ and $\boldsymbol{Z}_3 \in L_2[0,\infty)$. According to barbalat lemma $\boldsymbol{Z}_1$ converges to 0 when $t \to \infty$.